C. R. Chimie 16 (2013) 897–905

Contents lists available at SciVerse ScienceDirect

Comptes Rendus Chimie

www.sciencedirect.com

Full paper/Mémoire

Head-to-head and head-to-tail multilayer *n*-alkylsilsesquioxane films

Lingli Ni [a], Séverinne Rigolet [b], Abraham Chemtob [a,*], Céline Croutxé-Barghorn [a], Jocelyne Brendlé [b], Loïc Vidal [b]

[a] *Laboratory of Photochemistry and Macromolecular Engineering, ENSCMu, université de Haute-Alsace, 3, rue Alfred-Werner, 68093 Mulhouse cedex, France*

[b] *Institut de science des matériaux de Mulhouse, UMR CNRS 7361, ENSCMu, université de Haute-Alsace, 3, rue Alfred-Werner, 68093 Mulhouse cedex, France*

ARTICLE INFO

Article history:
Received 12 March 2013
Accepted after revision 30 May 2013
Available online 2 August 2013

Keywords:
Self-assembly
Sol–gel
Interdigitation
Photopolymerization
Solid-state NMR
Hybrid film

ABSTRACT

Two lamellar organosilica films made up of stacks of head-to-head and head-to-tail alkyl bilayers were synthesized by a UV-driven polymerization of *n*-$C_{18}H_{37}SiCl_3$ and *n*-$C_{18}H_{37}Si(OCH_3)_3$, respectively. In addition to thermogravimetry and small-angle X-ray scattering, the characterization of these multilayer systems was focused on a variety of multinuclear solid-state NMR methods (^1H, ^{29}Si, ^{13}C, 2D WISE). The chemical structure of the siloxane interlayer, the alkyl chain conformation and thermal stability were systematically investigated and compared. Through its marked sensitivity to molecular motion, solid-state NMR was used to investigate the effect of interdigitation on alkyl chain dynamics.

1. Introduction

Fluid lipid bilayer is the landmark structure of all biological membranes [1,2]. Lipids segregate within the membrane into different domains depending on their alkyl chain, head group and degree of saturation [3,4]. Saturated lipid molecules are unique for their ability to self-assemble into crystalline ordered domains because of the linear geometry of the alkane chains and the van der Waals interactions between methylene groups [5]. Their self-assembly ability has already resulted in numerous examples of artificial monolayer and bilayer films [6]. However, little has been reported on expanded multilayers, which upon successive addition of saturated lipid bilayers could stack to form non-fluid three-dimensional (3D) crystalline materials [7].

Non-lipid saturated amphiphiles appear to have been more successful to afford 3D lamellar films [8–11]. A very promising methodology relies on organosilane hybrid precursors of the structure: $H_3C(CH_2)_nSiX_3$ [12–17] and $X_3Si(CH_2)_nSiX_3$ [18,19] (X = alkoxy, Cl) that self-assemble into inorganic–organic multilayer structures. Hybrid materials with organic–inorganic character represent a very dynamic field of research [20,21]. Their novel properties and multifunctional nature has opened up many opportunities of applications in very different domains [22]. In particular, these lamellar hybrids represent attractive materials in polymer nanocomposites [22,23], catalysis [24], optoelectronics [12,25,26] and photolithography [27,28]. In contrast to the first class of metallic hybrid mesostructures forming spontaneously, the self-organization of alkylsilanes is triggered by concomitant hydrolysis and polycondensation of the reactive group X, referred to as the sol–gel process. Acid-catalyzed hydrolysis replaces the –SiX functions by –SiOH silanol functions, thus, driving the in situ generation

* Corresponding author.
E-mail address: abraham.chemtob@uha.fr (A. Chemtob).

1631-0748/$ – see front matter © 2013 Académie des sciences. Published by Elsevier Masson SAS. All rights reserved.
http://dx.doi.org/10.1016/j.crci.2013.05.017

of amphiphilic *n*-alkyltrisilanol species. Subsequent polycondensation reactions yield a cross-linked siloxane layers separating bilayered stacks of alkyl chains. In general, it is very difficult to achieve the long-range order of crystalline films with monosilylated precursors [29], and a more popular approach relies on symmetric bridged precursors [18,30–36]. The result is a very small number of studies reporting the lamellar structuring of *n*-alkylsilsesquioxane films, in this way, mimicking the organization of saturated lipids [12–19].

In 2011, we introduced an alternative UV-driven sol–gel process performed without solvent and water, enabling the formation of crystalline multilayer *n*-alkylsilsesquioxane films from trichloro- [37] or trimethoxy-based [38] monosilylated *n*-alkylsilanes. In our procedure, a photoacid generator ($(C_{12}H_{25})_2\Phi_2I^+SbF_6^-$) was solubilised into the precursor. Upon UV irradiation, the liberated $H^+SbF_6^-$ Brønsted superacids caused both the fast sol–gel photopolymerization and the self-assembly process. The important benefits of using a solvent-free pathway are to circumvent the long hydrocarbon chain insolubility and the solvation effect perturbing the self-assembly process. The resulting 3D lamellar structures with bilayered hydrocarbon chains exhibited a strong resemblance with crystalline lipid domains. A very intriguing feature, which serves as a starting point to this study, has been the possibility to tailor the alkyl packing arrangement, depending on the chemical nature of the anchoring group (*X*). As depicted in Fig. 1, we performed the photoacid-catalyzed sol–gel process of two *n*-octadecyl monosilylated precursors, which differ in the nature of the –SiX hydrolyzable function $-C_{18}H_{37}SiCl_3$ (C_{18}TCS) and $C_{18}H_{37}Si(OCH_3)_3$ (C_{18}TMS): the trichlorosilane derivative yielded a stacking of non-interpenetrated bilayers while the trimethoxysilane precursor favored an equivalent interdigitated structure, with alkyl chains of a first layer intercalated in the space between two chains of an opposing layer.

Our characterization effort was mainly focused on a combination of standard solid-state nuclear magnetic resonance (NMR) techniques: ^{1}H, ^{29}Si, ^{13}C, 2D WISE. The chemical structure of the siloxane and hydrocarbon sheets, the alkyl conformational order and thermal stability are all important issues that were systematically investigated and compared in the two mesostructures. Another goal of this study was to examine whether the bilayer arrangement has an effect on the alkyl chain dynamics. It seems intuitively plausible that an interdigitated mesostructure by constraining the mobility of the chain ends may reduce the extent of chain motion compared to a non-interpenetrated system. The dependency between dipolar couplings and the respective mobility and separation of the nuclei involved makes solid-state NMR a well-suited technique to assess the local dynamical properties of these polymeric structures [39,40].

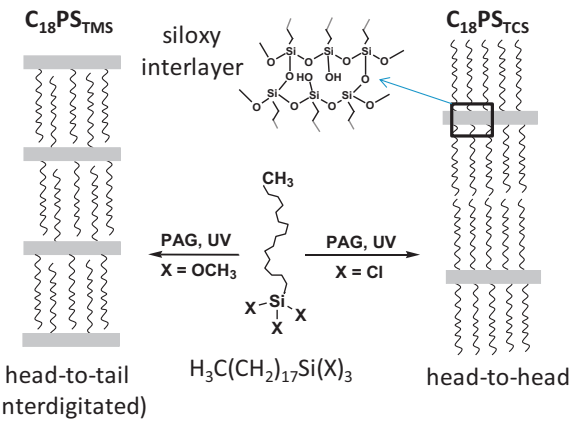

Fig. 1. Effect of the hydrolyzable group ($X = OCH_3$ or Cl) on the packing geometry of the lamellar *n*-octadecylsilsesquioxane mesostructure.

2. Experimental

2.1. Chemicals

n-Octadecyl trimethoxysilane (C_{18}TMS, 97% wt) and *n*-octadecyl trichlorosilane (C_{18}TCS, 97% wt) were purchased from ABCR. Benzophenone was used as a photosensitizer and the PAG UV 1241 (bis-dodecyl diphenyliodonium hexafluoroantimonate salt) were provided by Aldrich and Deuteron, respectively. All of the chemicals were used as received without further purification.

2.2. Synthesis of multilayer hybrid films based on C_{18}TMS and C_{18}TCS

In a typical procedure, photoacid generator UV1241 (2% wt) and benzophenone (2% wt) were dissolved in the C_{18}TMS or C_{18}TCS precursors to form a photolatent solution in the absence of UV light. The resulting formulation was then deposited on a glass substrate or silicon wafers (SAXS analysis) previously treated by a 20% wt NaOH solution using an Elcometer 4340 automatic film applicator equipped with a wire wound bar to produce a 5-μm-thick liquid film. Irradiation was performed at room temperature under a UV conveyor with a belt speed of 10 m/min using a UV lamp (H lamp, Fusion) with a light intensity of 1.46 J/cm^2 per pass. The C_{18}TMS and C_{18}TCS hybrid films were subjected to five successive passes under the conveyor to yield solid poly(*n*-alkylsilsesquioxane) films labelled as $C_{18}PS_{TCS}$ and $C_{18}PS_{TMS}$, respectively. During UV irradiation, the room's humidity rate was maintained between 30 and 35% as assessed with a hygrometer.

2.3. Characterization

X-ray diffraction patterns were obtained on a PANalytical X'pert Pro diffractometer with fixed slits using Cu Kα radiation ($\lambda = 1.5418$ Å) and θ–2θ mounting. Before analysis, films on silicon wafers were directly deposed on a stainless steel sample holder. Data were collected between 0.5 and 10° 2θ degrees with a scanning step of 0.01° s^{-1}. ^{13}C ($I = 1/2$) magic angle spinning (MAS) and ^{1}H–^{13}C cross polarization magic angle spinning (CP–MAS) NMR spectra were recorded with a Bruker double-channel 4-mm probe with a spinning frequency of 12 kHz on a Bruker Avance II

400 spectrometer operating at B_0 = 9.4 T (Larmor frequency ν_0 (^{13}C) = 100.63 MHz and ν_0 (^{1}H) = 400.17 MHz). ^{13}C single-pulse MAS NMR experiments were performed with a $\pi/4$ pulse duration of 2.5 μs and a 60 s recycling delay, these recording conditions ensuring the quantitative determination of the proportions of the different carbon species. Typically, 1000 scans were recorded. ^{1}H–^{13}C CPMAS NMR experiments were acquired using a ramp for Hartmann–Hahn matching with 8 s recycling delay and a contact time of 1 ms. The radiofrequency field strength used for ^{1}H decoupling was set at 66 kHz. For the variable-temperature CP-MAS experiments, the sample temperature was controlled to within ± 0.2 °C by a Bruker variable-temperature unit (BVT3000). Typically, 132 scans were recorded. ^{1}H–^{13}C HETCOR/WISE experiments were performed under the conditions of MAS. A ^{1}H 90° pulse of 5.1 μs was followed by a proton evolution period t_1 consisting of 256 increments of 20 μs. After each t_1 period, cross polarization (contact time = 1 ms) followed by carbon detection with continuous wave proton decoupling of 64 kHz gives a carbon spectrum that is modulated as a function of t_1 by free induction decay of the associated protons. The spectral widths were 28 and 200 kHz in F_1 and F_2 dimensions, respectively. Typically, 256 scans were taken for each slice, with a repetition time of 8 s.The processed data sets contained 1024 points in the F_2 (^{13}C) dimension and 256 points in the F_1 (^{1}H) dimension. ^{1}H (I = 1/2) MAS NMR experiments were performed at room temperature on a Bruker Avance II 400 spectrometer operating at B_0 = 9.4 T (Larmor frequency ν_0 = 400.17 MHz). Single-pulse experiments (SPE) were carried out with a double-channel 2.5-mm Bruker MAS probe, a spinning frequency of 30 kHz and a $\pi/2$ pulse duration of 3.5 μs. ^{1}H spin lattice relaxation times (T_1) were measured with the inversion-recovery pulse sequence for all samples. Typically, 64 scans were recorded. ^{29}Si (I = 1/2) ^{1}H–^{29}Si CP–MAS NMR spectra were recorded at room temperature, using a ramp for Hartmann–Hahn matching, 8 s recycling delay and a contact time of 4 ms, on a Bruker Avance II 300 spectrometer operating at B_0 = 7.1 T (Larmor frequency ν_0 (^{29}Si) = 59.62 MHz and ν_0 (^{1}H) = 300.13 MHz) with a Bruker double-channel 7-mm probe with a spinning frequency of 4 kHz. The radiofrequency field strength used for ^{1}H decoupling was set at 55 kHz. Typically, 1000 scans were recorded. Chemical shifts reported thereafter are relative to tetramethylsilane for ^{29}Si, ^{13}C and ^{1}H. Deconvolutions of the spectra were peformed using Dmfit software [41]. Thermally induced weight-loss curves were obtained through Q500 thermogravimetric analyzer (TA instruments) with a nitrogen flow of 20 mL/min; the temperature range was over 25–1000 °C at a heating rate of 5 °C/min.

3. Results

3.1. Small-angle X-Ray diffraction

Fig. 2 displays the X-ray diffraction patterns of the $C_{18}PS_{TCS}$ and $C_{18}PS_{TMS}$ hybrid films, derived respectively from C_{18}TCS and C_{18}TMS sol–gel photopolymerization. Both patterns are consistent with a multilayer mesostructure composed of alkyl chains bilayers separated by siloxane sheets. The presence of several peaks at the intermediate scattering angles suggests a long-range periodicity [42], although a relative broad 001 peak is observed in both structures (full width at half maximum of 2θ value of 0.11° and 0.20° for $C_{18}PS_{TCS}$ and $C_{18}PS_{TMS}$, respectively). The major difference between the two films prepared from alkoxy- and chloro- precursors appears in the position of the low-angle 001 peak, which is indicative of a distinct packing arrangement of the hydrocarbon chains forming the interior bilayer. Compared to the theoretical length of a fully extended $C_{18}H_{37}SiO_x$ unit (l = 2.62 nm), the d-spacing value of 5.08 nm ($\sim 2 \times l$) found with $C_{18}PS_{TCS}$ can be related to a conventional bilayer organization with a head-to-head arrangement. In the case of $C_{18}PS_{TMS}$, the distance of 2.73 nm, close to the theoretical chain length suggests distinctively fully interdigated bilayers with alternating up-and-down octadecyl chains. Well-defined strips are clearly observed through the TEM images of both samples (Fig. 2), which are consistent with a lamellar morphology. The inter-lamellar distances of 5.1 nm and 2.6 nm found with $C_{18}PS_{TCS}$ and $C_{18}PS_{TMS}$, respectively (utilizing Fourier transform for image processing), are quite close to those obtained by X-ray diffraction data. Differences in self-aggregation kinetics or in the size of the leaving group (OMe vs Cl) could be at the origin of the different chain packing. The wide-angle diffraction data shown in Supplementary data, Fig. S1 provides additional insight into the chain–chain spacing. The distances of 4.16 Å and 4.12 Å for $C_{18}PS_{TCS}$ and $C_{18}PS_{TMS}$ are close to those observed in dense solid phases of alkyl chains [13]. While the general mesoscopic organization of the hybrid films can be established through XRD and TEM analyses, information about composition, mobility and molecular interactions that form the basis of the self-assembled lamellar mesostructure was studied by a combination of solid-state NMR methods.

3.2. Solid-state NMR

3.2.1. ^{29}Si CP–MAS NMR

The partial condensation of the inorganic silica interlayer is clearly evidenced using ^{29}Si CP–MAS NMR. As shown in Fig. 3, the spectra of the irradiated samples $C_{18}PS_{TMS}$ and $C_{18}PS_{TCS}$ are dominated by T^2 ((HO)(R)-Si(OSi)$_2$, –58 ppm) and T^3 ((R)Si(OSi)$_3$, –68 ppm) siloxane species. Additional FT–IR analysis (not presented) revealed for both samples, a complete hydrolysis after the photo-irradiation process. Compared to $C_{18}PS_{TCS}$, the minor contribution of trisiloxane units (T^3) in $C_{18}PS_{TMS}$ indicates less condensed siloxane sheets, a result supported also by the presence of T^1 ((HO)$_2$(R)Si(OSi), –50 ppm) subspecies in this latter sample. The higher reactivity of the chlorosilyl functions compared to alkoxysilyl groups, presumably, accounts for the greater degree of condensation reached by $C_{18}PS_{TCS}$ [43]. On the other hand, the hydrolysis of the chlorosilyl moieties produces in situ HCl, which is able to catalyze condensation reactions and might also contribute to the formation of denser films. Quantitative single-pulse experiments (SPE) (not provided) revealed a tendency similar to that of the $C_{18}PS_{TMS}$ film, exhibiting a slightly less condensed structure (T^3: 52.3%, T^2: 47.7%) than the

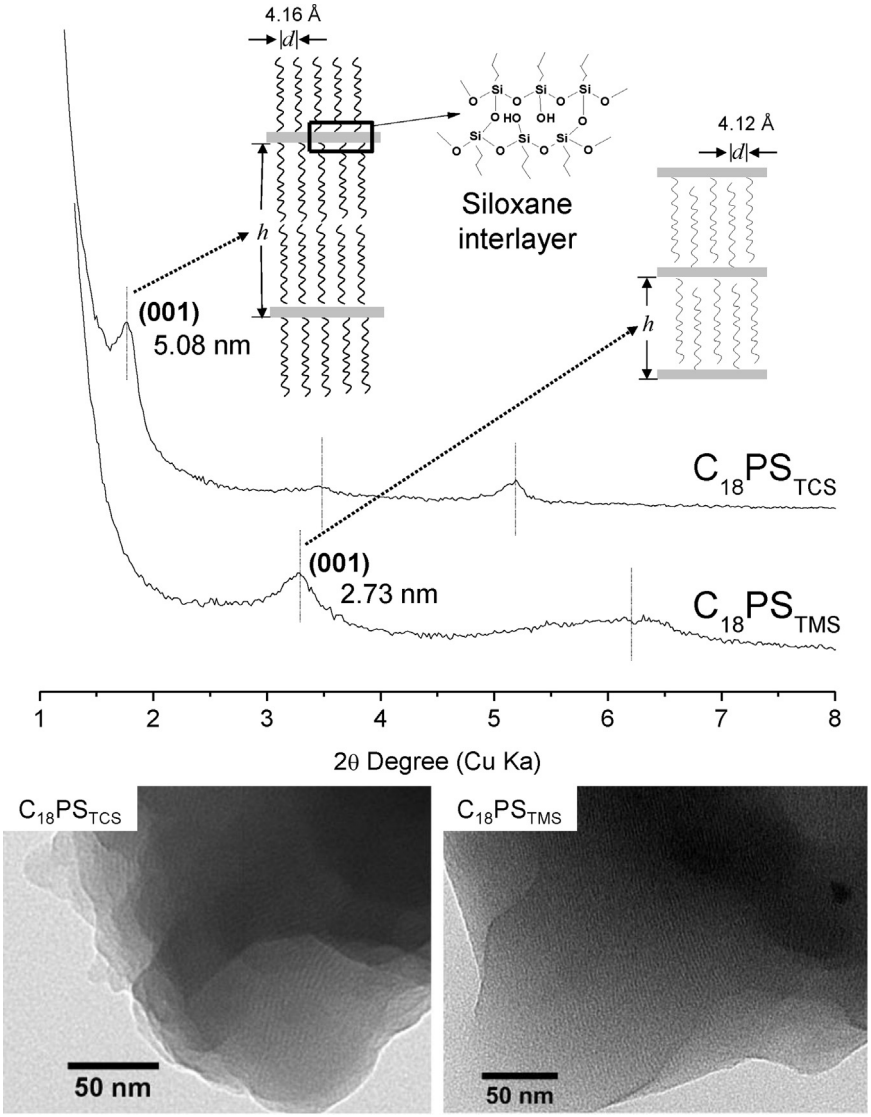

Fig. 2. (Top) XRD patterns of $C_{18}PS_{TCS}$ and $C_{18}PS_{TMS}$ hybrid lamellar films. A trend for interdigitation is evidenced in $C_{18}PS_{TMS}$ sample while $C_{18}PS_{TCS}$ is characterized by non-interpenetrated bilayers. (Bottom) TEM images showing the multilayered mesostructures.

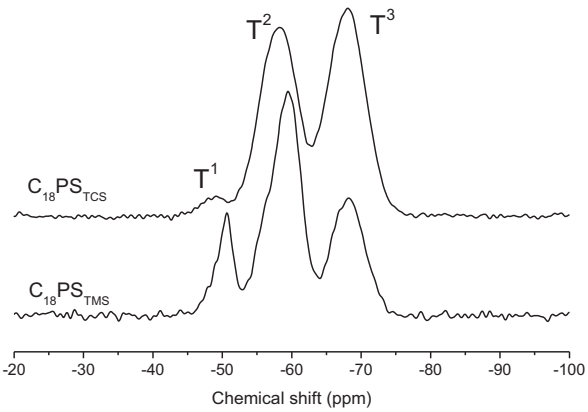

Fig. 3. ^{1}H–^{29}Si CP–MAS NMR spectra of the UV-cured $C_{18}PS_{TCS}$ and $C_{18}PS_{TMS}$ films.

$C_{18}PS_{TCS}$ film (T^3: 54.7%, T^2: 45.3%). As expected, the difference in condensation is less pronounced than in the CP–MAS experiment, thus, suggesting that this parameter is unlikely to be behind the variation in chain packing (Fig. 3).

3.2.2. ^{13}C CP– and SPE–MAS NMR

The *n*-octadecyl chain conformation and its thermal stability have been assessed by ^{13}C solid-state NMR for both precursors. Of particular interest in alkane-based compounds is indeed the internal methylene carbon region (C_3 to C_{16}) between 30 and 34 ppm, as shown in the CP–MAS spectra in Fig. 4. The other resonances at lower chemical shifts are assigned to tethering (C_1, C_2) and terminal (C_{17}, C_{18}) carbons [13]. The chemical shift of the inner methylene carbons is known to be sensitive to alkane chain conformation: the upfield (30.5 ppm) and downfield

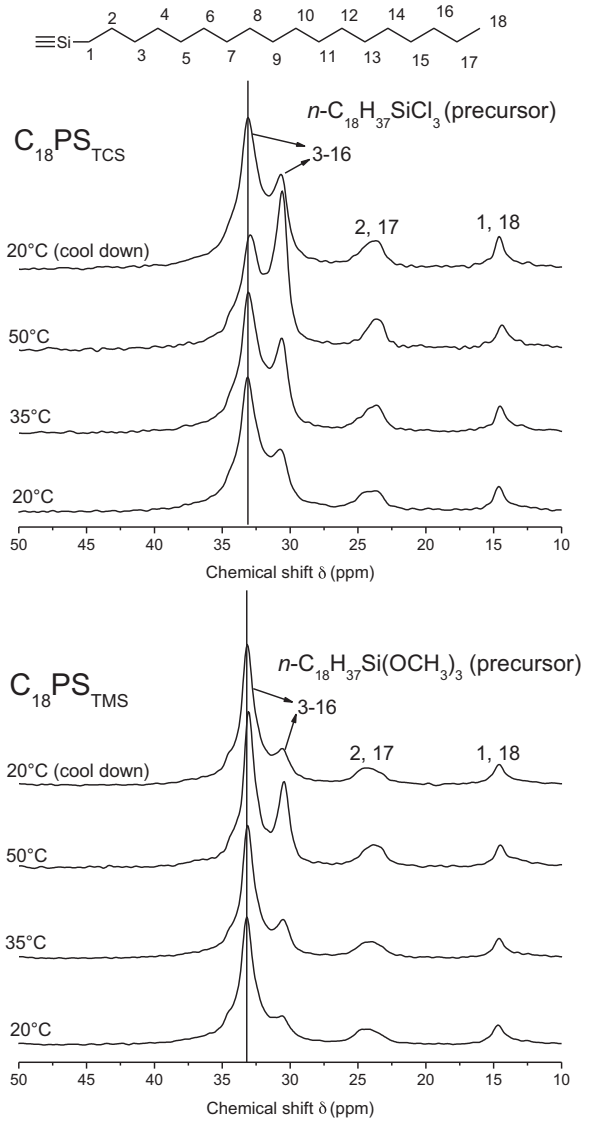

Fig. 4. ^{1}H–^{13}C CP-MAS NMR spectra of $C_{18}PS_{TCS}$ and $C_{18}PS_{TMS}$ at various temperatures showing the thermal stability of the two lamellar mesostructures.

(33.2 ppm) signals are attributed to *gauche* and *trans* conformers, respectively [44,45]. Therefore, it can be concluded that at ambient temperature, the $C_{18}PS_{TMS}$ film exhibits a higher conformational order than its chlorosilane analogue, even though the resonance of the *trans* signal remains prevalent in both films. Variable-temperature ^{13}C CP–MAS NMR have been implemented to probe the thermal stability of the octadecyl bilayer. Fig. 4 shows that upon heating, the *trans* component at 33 ppm diminishes and the 30 ppm signal associated with *gauche* defects increases. The disordering effect of temperature is much greater with $C_{18}PS_{TCS}$, with a higher proportion of chains becoming completely disordered at 50 °C, suggesting the lower thermal stability of this latter film. Accordingly, the disordering of the chains appears as a reversible process for the interdigitated structure, since the ^{13}C spectra of $C_{18}PS_{TMS}$ are observed to return to their original state upon cooling. By contrast, $C_{18}PS_{TCS}$ keeps a memory of the heat-induced disorder with a higher number of *gauche* defects upon returning to ambient temperature, further supporting the higher thermal stability of $C_{18}PS_{TMS}$.

In addition to ^{13}C chemical shifts, containing information about molecular structure and conformation, the shape of the resonances must be discussed in detail because they may give insight into the motional processes of the hydrocarbon chain. By creating spatial proximity between alkyl chains, interdigitation can possibly change the dynamic character of the chain-end terminal methyl (C_{18}) and that of the adjacent methylene (C_{17}). To assess the difference in molecular mobility between the two multilayer films, SPE instead of cross polarization (CP) experiments spectra should be preferably performed. In CP spectra, $^{1}H \rightarrow {}^{13}C$ magnetization transfer relies on the strength of the heteronuclear dipolar couplings, which decreases with fast motions. Consequently, the more mobile carbons located at the chain end, such as C_{17} or C_{18}, are significantly under-represented or barely detectable in a CP experiment. In contrast, SPE experiments should make the observations of these terminal carbons easier (as sharp spectral features) but require recycling delays of 60 s and then long experimental times for collecting a spectrum with a good signal-to-noise ratio [46]. The ^{13}C SPE–MAS NMR spectra of two self-assembled hybrid films are provided in Fig. 5.

As expected, the disordered *gauche* methylenes experiencing weak dipolar couplings are more represented in the SPE spectra.

In addition, narrow lines from mobile carbons now arise in the high-field range of the SPE spectra, whereas they are not seen in the CP spectra (Fig. 4). Unfortunately, the α-methylene carbon (C_{17}) adjacent to the terminal CH_3 arises in the ~24 ppm region, in which C_2 makes also a contribution. In both SPE spectra, the double maxima resonance can be decomposed into a broad and a sharp signal, whose proportions are very different. The sharp spectral feature is assumed to be essentially representative of mobile C_{17}, while the broad resonance is a mixed contribution from more rigid carbons (C_{17} and C_2) in the close vicinity of the Si atom. No quantitative interpretation is attempted here because the deconvolution is not unique, and consequently unreliable. The proposed idea is that this sharp line shape (intensity, width) could be used as a qualitative marker of C_{17} carbons' mobility. Clearly, the contribution of this narrow line is smaller and broader in $C_{18}PS_{TMS}$ compared to $C_{18}PS_{TCS}$. Consequently, such a difference may be the sign of a higher mobility restriction of the α-methylenes carbons imposed by the interdigitation of the alkyl chains in $C_{18}PS_{TMS}$.

Likewise, the carbon C_{18} and tethering carbon C_1 are not well resolved in both SPE spectra and appear in the 14 ppm region as the sum of a broad and a sharp component with different relative areas. Again, we assume that the narrow line arises mainly from the most mobile terminal methyl groups (C_{18}), whereas the broad resonance originates from carbon C_1 attached to the rigid siloxane network and more rigid C_{18} carbons. In the SPE spectra, it is clear that the

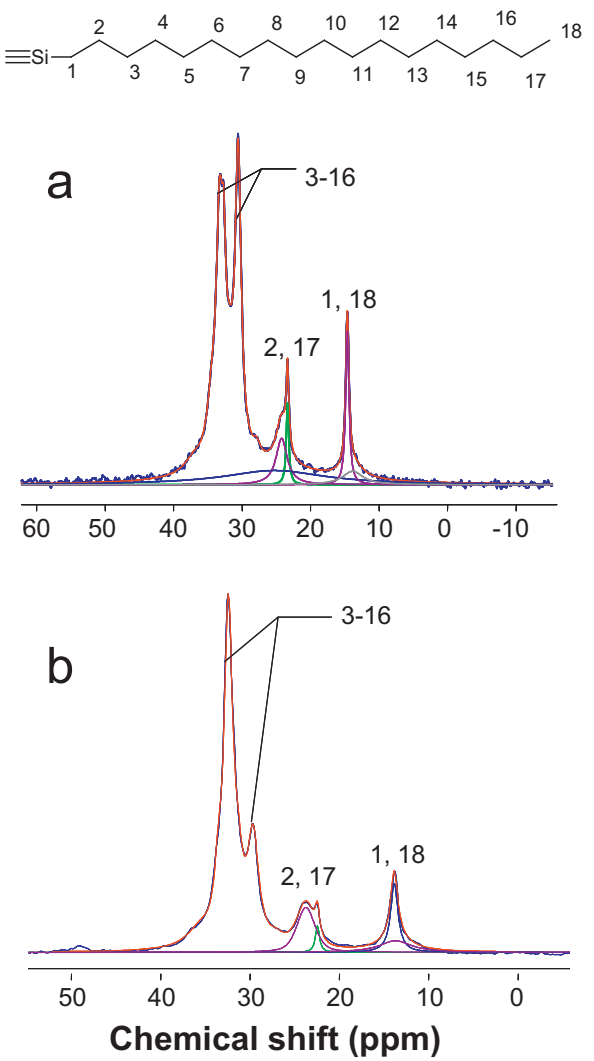

Fig. 5. ^{13}C SPE–MAS NMR spectra of the $C_{18}PS_{TCS}$ (a) and $C_{18}PS_{TMS}$ (b) films. Color available on line.

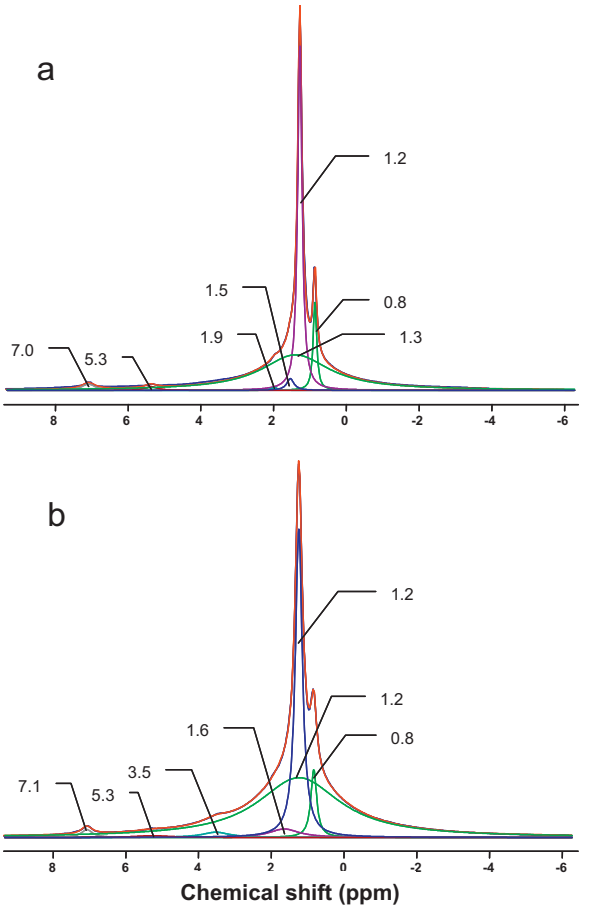

Fig. 6. ^{1}H MAS NMR spectra of $C_{18}PS_{TCS}$ (a) and $C_{18}PS_{TMS}$ (b). To complete the proton assignment, we note the weakly intense signals at 1.9 ppm (0.4%) and 1.6 ppm (3.2%) in $C_{18}PS_{TCS}$ and $C_{18}PS_{TMS}$, respectively, assigned to isolated non-hydrogen-bonded silanols. Two other spectral features attributed to hydrogen-bonded hydroxyls (silanol, physisorbed water) are detected in $C_{18}PS_{TMS}$ at 3.5 ppm (1.8%) and 5.3 ppm (0.7%) – where a higher chemical shift reflects stronger interactions – instead of a single one in $C_{18}PS_{TCS}$ at 5.3 ppm (1%). The overall higher population in silanols found in $C_{18}PS_{TMS}$ agrees with its lower degree of condensation, already evidenced by ^{29}Si solid-state NMR. The last small spectral features at 7.0 ppm ($C_{18}PS_{TCS}$) and 7.1 ppm ($C_{18}PS_{TMS}$) were ascribed to the aromatic protons from the photoacid generator ($(C_{12}H_{25})_2\Phi_2I^+PF_6^-$) and the photosensitizer ($\Phi_2C{=}O$). Color available on line.

interpenetrated $C_{18}PS_{TMS}$ film is characterized by a decreased contribution of the sharp line, which appears also narrower in comparison with $C_{18}PS_{TCS}$. Such qualitative difference might be indicative of a lower fraction in mobile terminal methyl groups in $C_{18}PS_{TMS}$, which is in accordance with the previous interpretation on C_{17}.

Even though the latter results are consistent with chain end mobility restrictions resulting from interdigitation, both samples also differ in conformational order. It is not unlikely, from our point of view, that the higher proportion of *trans* segments found in $C_{18}PS_{TMS}$ may also limit the motions of the α-methylenes and the terminal methyl groups. In contrast, we think that the weak difference in the degree of condensation of the siloxane interlayer is less likely to affect the mobility of the chain ends.

3.2.3. ^{1}H-MAS NMR

In the ^{1}H-MAS NMR spectra displayed in Fig. 6, the double maximum signal is readily assigned to CH_3 (∼0.8 ppm) and CH_2 (∼1.2 ppm) protons. In contrast to the ^{13}C spectrum, it is not possible to distinguish the α-methylene. However, the signal at 1.2 ppm, representative of all the methylene carbons, is again decomposable into a sharp and a broad component, whose relative contribution will depend on the rigidity of their environment. As expected, the methylenes in the interdigitated octadecyl chains ($C_{18}PS_{TMS}$) are characterized by an increased fraction of the broad feature (1.2 ppm, 59%) compared to $C_{18}PS_{TCS}$ (1.3 ppm, 52%), originating from the most tightly dipolarly coupled protons, lacking of mobility. In agreement with the ^{13}C SPE–MAS data, a lower mobility of the terminal methyl in $C_{18}PS_{TMS}$ is evidenced by a significantly broader resonance at 0.8 ppm with $\Delta\omega_{1/2} = 75$ kHz (45 kHz with $C_{18}TCS$). The rest of the proton assignment is discussed in the caption of Fig. 6.

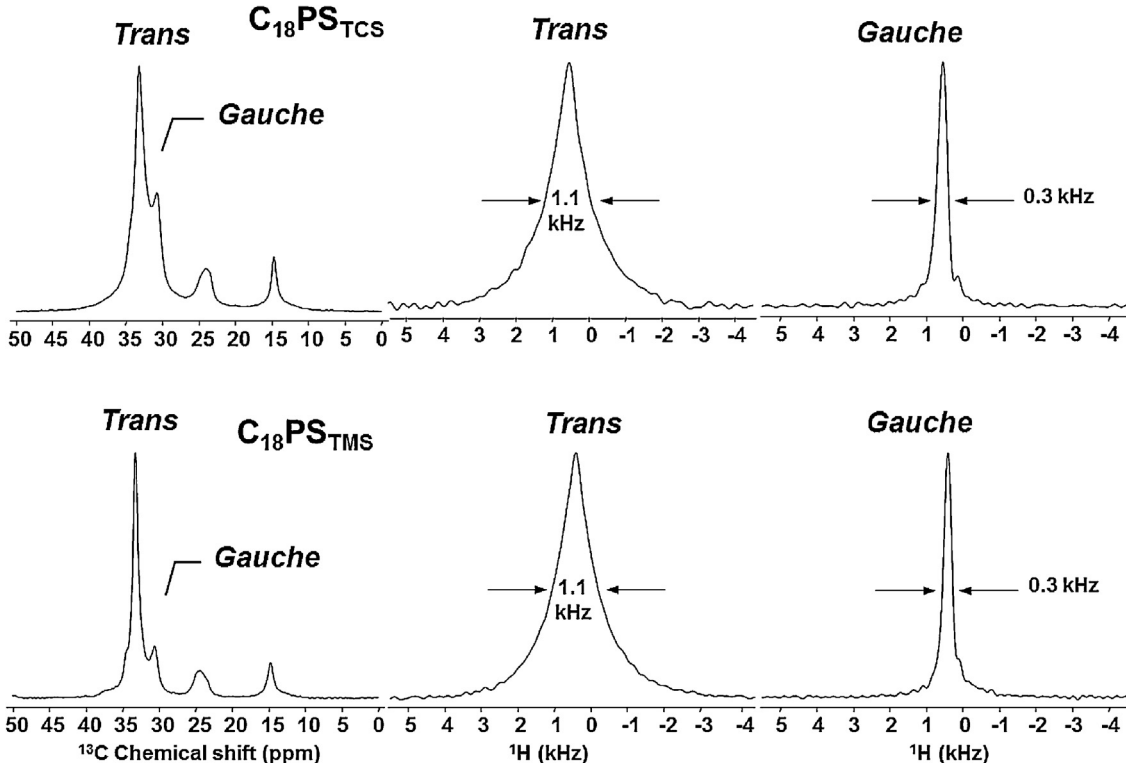

Fig. 7. ^{13}C CP MAS recorded at room temperature and ^{1}H wide-line spectra of $C_{18}PS_{TCS}$ and $C_{18}PS_{TMS}$. The ^{1}H wide-line spectra shown correspond to the ^{1}H slices of *gauche* and *trans* components at 30 and 33 ppm, respectively in the ^{13}C dimension in the 2D wide-line separation experiments (WISE).

3.2.4. 2D ^{1}H–^{13}C WISE NMR

Qualitative information about hydrocarbon chain molecular motion can be obtained by combining proton line width measurements with ^{13}C detection in a 2D NMR experiment commonly referred to as WIde-line SEparation (WISE) [47]. Indeed, it is a general principle that the proton line width characterizes the strength of the dipolar coupling among protons, which is strongly correlated with their local dynamics. For example, crystalline or rigid segments are known to increase the homonuclear dipolar interactions, leading to broad proton line width. Conversely, flexible or disordered regions are manifested by a substantial sharpening of the proton resonance, since the dipolar coupling is almost averaged out by fast molecular motions. The WISE technique has been introduced initially in the characterization of polymer to address dynamic heterogeneities caused by the coexistence of rigid and flexible moieties in the same macromolecule [48,49]. More recently, 2D WISE spectra were used to assess the chain mobility in self-assembled monolayers (SAM) [50,51].

The 2D WISE NMR spectra have been recorded for $C_{18}PS_{TCS}$ and $C_{18}PS_{TMS}$. In the ^{13}C NMR spectra displayed in Fig. 7, both films show different components at 33 and 30 ppm in the ^{13}C NMR spectra related to *trans* and *gauche* conformers respectively. Since the ^{13}C chemical shift is sensitive to conformation, slices taken of the ^{1}H dimension in a 2D WISE spectrum allow the separation of the broad proton resonances for ordered and disordered regions, which would completely overlap in a 1D ^{1}H NMR spectrum. These slices in the ^{1}H dimension for the methylene carbons at 33 ppm and 30 ppm are given in Fig. 7. (The full 2D WISE NMR spectra are shown in Supplementary data, Fig. S2). As expected from the larger dipolar couplings of conformationally ordered chains, the ^{1}H slices of the 33 ppm methylene signal display a broader line (1.1 kHz) than that of the gauche resonance at 30 ppm (0.3 kHz). However, both films have essentially the same dipolar slices at 33 and 30 ppm. Such a remarkable result implies that it is not possible to detect mobility differences of the *inner* methylenes (C_3–C_{16}), whether *trans* or *gauche*, depending on their packing geometry. Presumably, the cohesive interactions developed in an interdigitated structure do not provide any additional mobility restriction, which could induce a detectable increase in the dipolar coupling. Nevertheless, one must bear in mind that only a part of the ^{13}C nuclei can be observed with a 2D-WISE experiment based on CP data. With regards to the terminal methyl, the 14 ppm peak contains contributions from carbons 1 and 18, and cannot be used to draw conclusions on methyl dynamics.

3.3. Thermal gravimetric analysis

In Fig. 8, the TGA thermograms of $C_{18}PS_{TMS}$ and $C_{18}PS_{TCS}$ show respectively two and three discernible weight-loss regions. The small transition initiated at ~105 °C, found in both films, can be related to the loss of physisorbed water and the progressive post-condensation of residual silanols,

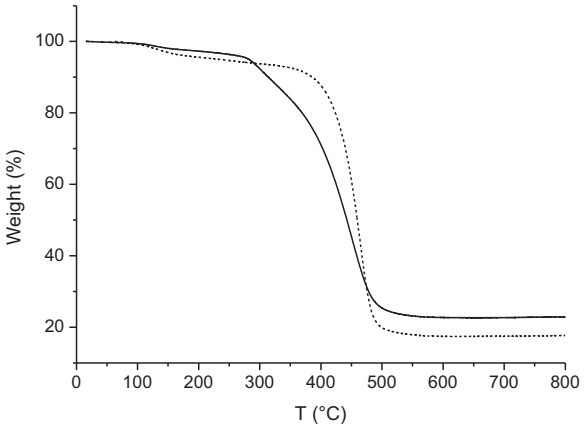

Fig. 8. Thermogravimetric analysis of $C_{18}PS_{TCS}$ (—) and $C_{18}PS_{TMS}$ (——).

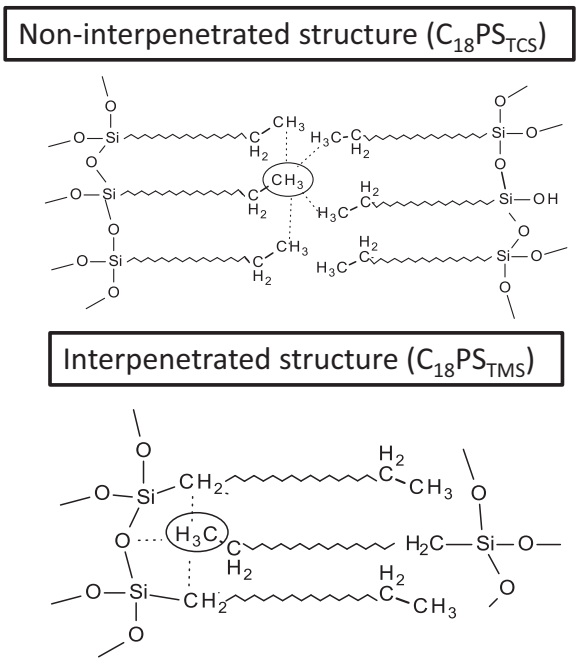

Fig. 9. Local and mesoscopic structures of the two *n*-alkylsilsesquioxane films differing in the packing geometry of the alkyl tail. The two configurations show the effect of the alkyl chain interdigitation on the local environment of the CH_3 and α–CH_2 groups.

liberating new water molecules [13]. The slowly decreasing slope suggests that silanol condensation reactions are effective over a wide range of temperatures, from 105 to 300 °C approximately. For this first small transition, the larger weight-loss noted in $C_{18}PS_{TCS}$ is not consistent, a priori, with its more condensed siloxane network. This suggests the hypothesis of a lower temperature degradation of the disordered octadecyl chains, which are significantly represented in this latter sample. Consequently, the bimodal population in *gauche* and *trans* conformers in $C_{18}PS_{TCS}$ could account for the existence of two distinct large transitions at 280 and 350 °C, marking the degradation of the alkyl chain. The progressive and low-temperature transition may be assigned to *gauche* defects displaying a lower thermal stability and a range of possible conformations. The higher temperature transition is sharper, which is in agreement with ordered *trans* alkyl chains with a single conformation. Accordingly, the degradation of high *trans* conformers populations in $C_{18}PS_{TMS}$ leads to a single sharp transition at a similar temperature of 350 °C. The final weight-losses of $C_{18}PS_{TCS}$ (22%) and $C_{18}PS_{TMS}$ (18%) observed at high temperature are consistent with the theoretical values of the Si–O–Si moiety, around 17%.

4. Conclusion

We have taken advantage of an original sol–gel photopolymerization process to generate two multilayer poly(*n*-octadecylsiloxane) films characterized by a different arrangement of the alkyl bilayer. A head-to-head geometry was favoured by the self-assembly of $C_{18}TCS$ whereas a head-to-tail configuration was preferentially formed with $C_{18}TMS$. On the basis of various characterization techniques (SAXS, MAS NMR methods), we proved that $C_{18}PS_{TMS}$ differed in the interdigitation of the alkyl bilayers, a higher *trans* population, and a slightly lower siloxane condensation, in comparison with $C_{18}PS_{TCS}$. The ^{13}C SPE–MAS NMR spectra established a lower mobility for the α-methylene carbons (C_{17}) and the methyl chain ends (C_{18}) in this interpenetrated structure, a result confirmed by ^{1}H MAS NMR in the case of the terminal methyl group. As illustrated in Fig. 9, C_{17} and C_{18} are parts of the alkyl chain whose local environment is most likely to be affected by the packing arrangement. In an interdigitated structure, these headgroups are surrounded by stiff methylene groups (tethering C_1 carbon) and the cross-linked siloxane of the opposite layer. This is in sharp contrast with their local environment in a non-interpenetrated mesostructure that is much more mobile. We suggest that mobility difference is to be expected for reasons of (a) interdigitation, but also (b) conformational ordering, and to a less extent, (c) the overall density of the siloxane interlayer. Obviously, we cannot separate all of the above contributions and claim that the interdigitated environment is a single source of a stronger immobilization of the hydrocarbon chains. Future studies including *n*-alkylsilane alkoxides functionalized at their chain end by CF_3 or PO_3H_2 groups should provide new insights into the structural and dynamic processes of these supramolecular materials [52].

Appendix A. Supplementary data

Supplementary data associated with this article can be found, in the online version, at http://dx.doi.org/10.1016/j.crci.2013.05.017.

References

[1] X. Zhang, J. Shen, Adv. Mater. 11 (1999) 1139.
[2] R. Ziblat, L. Leiserowitz, L. Addadi, Angew. Chem. Int. Ed. 50 (2011) 3576.
[3] I. Kuzmenko, H. Rapaport, K. Kjaer, J. Als-Nielsen, I. Weissbuch, M. Lahav, L. Leiserowitz, Chem. Rev. 101 (2001) 1659.

[4] D.M. Small, J. Lipid Res. 25 (1984) 1490.
[5] S.M. Gruner, J. Phys. Chem. 93 (1989) 7562.
[6] I. Kuzmenko, M. Kindermann, K. Kjaer, P.B. Howes, J. Als-Nielsen, R.G. Granek, v. Kiedrowski, L. Leiserowitz, M. Lahav, J. Am. Chem. Soc. 123 (2001) 3771.
[7] S.L. Souza, M. José Capitàn, J. Alvarez, S.S. Funari, M.H. Lameiro, E. Melo, J. Phys. Chem. B 113 (2009) 1367.
[8] C.C. Evans, L. Sukarto, M.D. Ward, J. Am. Chem. Soc. 121 (1998) 320.
[9] V.A. Russell, M.C. Etter, M.D. Ward, J. Am. Chem. Soc. 116 (1994) 1941.
[10] J.A. Swift, A.M. Pivovar, A.M. Reynolds, M.D. Ward, J. Am. Chem. Soc. 120 (1998) 5887.
[11] A. Ulman, Chem. Rev. 96 (1996) 1533.
[12] A.B. Bourlinos, S.R. Chowdhury, D.D. Jiang, Y.-U. An, Q. Zhang, L.A. Archer, E.P. Giannelis, Small 1 (2005) 80.
[13] A.N. Parikh, M.A. Schivley, E. Koo, K. Seshadri, D. Aurentz, K. Mueller, D.L. Allara, J. Am. Chem. Soc. 119 (1997) 3135.
[14] A. Shimojima, K. Kuroda, Chem. Rec. 6 (2006) 53.
[15] A. Shimojima, Y. Sugahara, K. Kuroda, Bull. Chem. Soc. Jpn. 70 (1997) 2847.
[16] K. Fujii, T. Fujita, N. Iyi, H. Kodama, K. Kitamura, J. Mater. Sci. Lett. 22 (2003) 1459.
[17] Q.P. Ke, G.L. Li, Y. Liu, T. He, X.M. Li, Langmuir 26 (2009) 3579.
[18] J. Alauzun, A. Mehdi, C. Reyé, R.J.P. Corriu, J. Mater. Chem. 15 (2005) 841.
[19] F. Lerouge, G. Cerveau, R.J.P. Corriu, New J. Chem. 30 (2006) 1364.
[20] H. Zou, S. Wu, J. Shen, Chem. Rev. 108 (2008) 3893.
[21] C. Sanchez, L. Rozes, F. Ribot, C. Laberty-Robert, L. Grosso, Sassoye, Boissiere, L. Nicole, C. R. Chimie 13 (2010) 3.
[22] C. Sanchez, P. Belleville, M. Popall, L. Nicole, Chem. Soc. Rev. 40 (2011) 696.
[23] W.L. Ijdo, T. Lee, T.J. Pinnavaia, Adv. Mater. 8 (1996) 79.
[24] J. Alauzun, A. Mehdi, C. Reye, R.J.P. Corriu, Chem. Commun. (2006) 347.
[25] H. Peng, Y. Zhu, D.E. Peterson, Y. Lu, Adv. Mater. 20 (2008) 1199.
[26] M. Takahashi, C. Figus, T. Kichob, S. Enzo, M. Casula, M. Valentini, P. Innocenzi, Adv. Mater. 21 (2009) 1732.
[27] C.S. Dulcey, J.H. Georger, M.-S. Chem, S.W. MacElvany, C.E. O'Ferral, V.I. Benezra, J.M. Calvert, Langmuir 12 (1996) 1638.
[28] X. Sallenave, O.J. Dautel, G. Wantz, P. Valvin, J.-P. Lère-Porte, J.J.E. Moreau, Adv. Funct. Mater. 19 (2009) 404.
[29] S. Fujita, S. Inagaki, Chem. Mater. 20 (2008) 891.
[30] J.J.E. Moreau, B.P. Pichon, M. Wong Chi Man, C. Bied, H. Pritzkow, J.L. Bantignies, P. Dieudonné, J.L. Sauvajol, Angew. Chem. Int. Ed. 43 (2004) 203.
[31] J.J.E. Moreau, L. Vellutini, M. Wong Chi Man, C. Bied, J.L. Bantignies, P. Dieudonné, J.L. Sauvajol, J. Am. Chem. Soc. 123 (2001) 7957.
[32] J.J.E. Moreau, L. Vellutini, M. Wong Chi Man, C. Bied, P. Dieudonné, J.L. Bantignies, J.L. Sauvajol, Chem. Eur. J. 11 (2005) 1527.
[33] N. Liu, K. Yu, B. Smarsly, D.R. Dunphy, Y.-B. Jiang, C.J. Brinker, J. Am. Chem. Soc. 124 (2002) 14540.
[34] E. Besson, A. Mehdi, C. Reye, P. Gaveau, R.J.P. Corriu, Dalton Trans. 39 (2010) 7534.
[35] L.D. Carlos, V. De Zea Bermudez, V.S. Amaral, S.C. Nunes, N.J.O. Silva, R.A. Sa Ferreira, J. Rocha, C.V. Santilli, D. Ostrovskii, Adv. Mater. 19 (2007) 341.
[36] H. Tang, J. Sun, J. Jiang, X. Zhou, T. Hu, P. Xie, R. Zhang, J. Am. Chem. Soc. 124 (2002) 10482.
[37] A. Chemtob, L. Ni, A. Demarest, C. Croutxe-Barghorn, L. Vidal, J. Brendlé, S. Rigolet, Langmuir 27 (2011) 12621.
[38] L. Ni, A. Chemtob, C. Croutxe-Barghorn, L. Vidal, J. Brendlé, S. Rigolet, J. Mater. Chem. 22 (2012) 643.
[39] K. Schmidt-Rohr, H.W. Spiess, Multidimensional Solid-State NMR and Polymers, Academic Press, New York, 1994.
[40] N.A. Melosh, P. Lipic, F.S. Bates, F. Wudl, G.D. Stucky, G.H. Fredrickson, B.F. Chmelka, Macromolecules 32 (1999) 4332.
[41] D. Massiot, F. Fayon, M. Capron, I. King, S. Le Calve, B. Alonso, J.-O. Durand, B. Bujoli, Z. Gan, G. Hoatson, Magn. Reson. Chem. 40 (2002) 70.
[42] Y. Fujimoto, A. Shimojima, K. Kuroda, Chem. Mater. 15 (2003) 4768.
[43] D.A. Loy, B.M. Baugher, C.R. Baugher, D.A. Schneider, K. Rahimian, Chem. Mater. 12 (2000) 3624.
[44] W.L. Earl, D.L. VanderHart, Macromolecules 12 (1979) 762.
[45] W. Gao, L. Reven, Langmuir 11 (1995) 1860.
[46] M. Pursch, D.L. Vanderhart, L.C. Sander, G. Xiaohong, T. Nguyen, S.A. Wise, D.A. Gajewski, J. Am. Chem. Soc. 122 (2000) 6997.
[47] K. Schmidt-Rohr, J. Clauss, H.W. Spiess, Macromolecules 25 (1992) 3273.
[48] J. Clauss, K. Schmidt-Rohr, A. Adam, C. Boeffel, H.W. Spiess, Macromolecules 25 (1992) 5208.
[49] S.C. Kuebler, D.J. Schaefer, C. Boeffel, U. Pawelzik, H.W. Spiess, Macromolecules 30 (1997) 6597.
[50] S. Pawsey, K. Yach, J. Halla, L. Reven, Langmuir 16 (2000) 3294.
[51] H. Schmitt, A. Badia, L. Dickinson, L. Reven, B. Lennox, Adv. Mater. 10 (1998) 475.
[52] M. Geppi, S. Borsacchi, G. Mollica, C.A. Veracini, Appl. Spectrosc. Rev. 44 (2009) 1.